University of Groningen

Tin-lead-metal halide perovskite solar cells with enhanced crystallinity and efficiency by addition of fluorinated long organic cation

Pitaro, Matteo; Pau, Riccardo; Duim, Herman; Mertens, Martijn; Van Gompel, Wouter T.M.; Portale, Giuseppe; Lutsen, Laurence; Loi, Maria Antonietta

Link to publication in University of Groningen/UMCG research database

Tin-lead-metal halide perovskite solar cells with enhanced crystallinity and efficiency by addition of fluorinated long organic cation Ⓕ

ⓘD **Matteo Pitaro,** ⓘD **Riccardo Pau,** ⓘD **Herman Duim, et al.**

COLLECTIONS

Paper published as part of the special topic on Energy Storage and Conversion

Ⓕ   This paper was selected as Featured

🌐
View Online

⬆
Export Citation

◉
CrossMark

ARTICLES YOU MAY BE INTERESTED IN

Detailed Balance Limit of Efficiency of p-n Junction Solar Cells
Journal of Applied Physics **32**, 510 (1961); https://doi.org/10.1063/1.1736034

Recent progress and future prospects of perovskite tandem solar cells
Applied Physics Reviews **8**, 041307 (2021); https://doi.org/10.1063/5.0061483

Revealing the doping density in perovskite solar cells and its impact on device performance
Applied Physics Reviews **9**, 021409 (2022); https://doi.org/10.1063/5.0085286

AIP Publishing

Tin-lead-metal halide perovskite solar cells with enhanced crystallinity and efficiency by addition of fluorinated long organic cation ⓕ

Matteo Pitaro,[1] ⓘⒹ Riccardo Pau,[1,2] ⓘⒹ Herman Duim,[1] ⓘⒹ Martijn Mertens,[3] ⓘⒹ Wouter T. M. Van Gompel,[3] ⓘⒹ
Giuseppe Portale,[4] ⓘⒹ Laurence Lutsen,[3,5] ⓘⒹ and Maria Antonietta Loi[1,a] ⓘⒹ

AFFILIATIONS

[1]Photophysics and OptoElectronics Group, Zernike Institute for Advanced Materials, University of Groningen, Nijenborgh 4,
9747 AG Groningen, The Netherlands
[2]Dipartimento di Fisica, Università di Cagliari, Monserrato I-09042, Italy
[3]Hybrid Materials Design (HyMaD), Institute for Materials Research (IMO-IMOMEC), Hasselt University, Martelarenlaan 42,
B-3500 Hasselt, Belgium
[4]Macromolecular Chemistry and New Polymeric Material, Zernike Institute for Advanced Materials, University of Groningen,
Nijenborgh 4, 9747 AG Groningen, The Netherlands
[5]IMEC, Associated Laboratory IMOMEC, Wetenschapspark 1, B-3590 Diepenbeek, Belgium

Note: This paper is part of the special collection on Energy Storage and Conversion.
[a]Author to whom correspondence should be addressed: M.A.Loi@rug.nl

ABSTRACT

Highly performing mixed Sn/Pb-metal halide perovskite solar cells (PSCs) are among the most promising options to reduce Pb content in perovskite devices and enable, owing to their reduced bandgap, the fabrication of all-perovskite tandem solar cells. Whereas pure-Pb perovskite devices exhibit efficiency up to 25.5%, alongside a high open-circuit voltage ($\approx$1.2 V), Sn-Pb PSCs still show lower performances (22.2%) due to higher open-circuit voltage losses. Here, we introduced 2,3,4,5,6-pentafluorophenethylammonium cations in a perovskite active layer of composition $(FASnI_3)_{0.5}(MAPbI_3)_{0.5}$ to obtain highly oriented films with improved thermal stability. The treated films exhibit merged grains with no evidence of 2D structures, which could help to reduce the trap state density at the surface and grain boundaries. Solar cells fabricated with the fluorinated cation added to the active layer displayed reduced trap-assisted recombination losses and lower background carrier density, which leads to enhanced open-circuit voltages with respect to the reference samples and the active layers incorporating unfluorinated phenethylammonium cations. The best device reached an efficiency of 19.13%, with an open-circuit voltage of 0.84 V, which is substantially improved with respect to the reference sample showing 17.47% efficiency and 0.77 V open-circuit voltage. More importantly, the fluorinated cations' addition is instrumental to improve the device's thermal stability; 90.3% of the solar cell initial efficiency is maintained after 90 min of thermal stress at 85 °C in a nitrogen atmosphere.

I. INTRODUCTION

Metal halide perovskites (HP) have attracted massive interest from the scientific community in the last 12 years owing to their excellent absorption coefficient,[1] long charge carrier diffusion length,[2] small exciton binding energy,[3] and high charge carrier mobilities,[4] which make them extremely attractive as active layers for optoelectronic devices. Nevertheless, it is predominantly for their use in solar cells (SCs) that the attention of a large world-wide community has been focused on these materials. Pb-based compounds have been intensely studied as active

layer in single junction solar cells, exhibiting an astonishing record power conversion efficiency (PCE) of 25.7%, approaching closely the performance of single crystalline silicon solar cells (26.7%).[5,6] However, the presence of a significant amount of Pb in these materials, accompanied by the ionic nature of the chemical bonds involved, raises concerns about the environmental and human toxicity,[7] which ultimately could hamper the commercialization of perovskite solar cell (PSC) (HP-SC) devices.

To address these issues, research attention has recently shifted to lowering the Pb-content in HP-SCs by using alternative metals.

Tin turned out to be the most fitting candidate to fabricate Pb-free PSCs, considering the similar electronic configuration to that of lead and the closest similarity in size. Moreover, halide perovskite based on tin exhibits high optical absorption and excellent charge carrier transport.[8]

Nevertheless, Sn-based perovskite solar cells up to date have shown limited efficiency, mainly due to the intrinsic Sn-vacancies and Sn^{2+} oxidation that create a self p-doping of the material, which has been shown to be one of the factors limiting device performance.[9] In the last few years, an extensive effort has been made to reduce Sn^{4+} formation in Sn-based perovskite thin films. One of the most successful methods involves the addition of a small amount of 2D metal halide perovskites in the 3D perovskite precursors mixtures, which results in an effective reduction of Sn^{2+} oxidation.[10] The application of this method together with surface passivation protocols has led to the record efficiency of 14.81% for fully Sn-based solar cell.[11]

An important physical property of a solar cell's active layer material is its bandgap. The one of lead iodide-based perovskite lies between 1.45 and 1.55 eV, depending on the A site cation that is used.[12] According to the Shockley–Queisser limit, to maximize the single junction solar cell performances, the ideal bandgap should be somewhat lower between 1.2 and 1.4 eV. Different authors observed a bandgap bowing when Pb^{2+} cations are partially substituted by Sn^{2+}, which lowers the bandgap from 1.5 to 1.2 eV.[13] Therefore, the mixed Sn/Pb-perovskite is not only an ideal material for single junction devices but is also suitable as a back cell in an all-perovskite tandem device.[14] Furthermore, the presence of Pb promotes the so-called self-passivating effect,[15] which increases the stability of the HP-SC and reduces Sn^{2+} oxidation, and consequently, the self p-doping.[16,17] Despite their high current density ($\sim$32 mA cm^{-2})[18] owing to their narrower bandgap, single junction of mixed Sn/Pb-HP-SCs exhibit a lower power conversion efficiency (21.74%)[18] than Pb-based HP-SC. The lower performances of mixed Sn/Pb-based devices are mainly related to the large open-circuit voltage (V_{OC}) loss (0.3 V),[19] which has been attributed to short carrier lifetime,[12] high trap state density,[16] and the rapid oxidation of Sn^{2+}.[14,20,21] Recently, the addition of bulky organic cations [phenethylammonium, 3-(aminomethyl)piperidinium, and formamidine sulfinic acid] has been widely used to reduce the Sn^{4+} formation and to passivate both the electron-donating and electron-accepting defects at the grain boundaries.[21–23] This strategy led to an enhancement in the V_{OC} from 0.77 to 0.88 V.[23] The efficacy of the use of bulky organic cations to enhance PCE and V_{OC} of perovskite solar cells was underlined by Hayase's group,[18] who implemented a post-treatment passivation method using ethylenediamine (EDA). These authors demonstrated that EDA could lower the Sn^{4+} content by bonding with uncoordinated Sn and passivating the I^- vacancies present on the perovskite surface. Furthermore, by introducing Br^- anions in the Pb/Sn perovskite, they reached a record efficiency of 21.74% with a V_{OC} of 0.86 V and 0.39 V V_{OC} loss.

Recently, Lin et al.[24] explored the dynamic process of passivator adsorption on grain surfaces of phenethylammonium, phenylammonium, and 4-trifluoromethyl-phenethylammonium (CF3-PA). The authors claimed that 2D perovskite, Lewis bases/acids, and Zwitterions have an insufficient defect passivation, where a certain amount of surface area remains un-passivated due to the incomplete passivating agent adsorption into the defective sites during the film formation. The CF3-PA cations possess an enhanced adsorption into the defective sites on grain surface during the film crystallization, assuring a complete passivation. The champion device exhibited a PCE of 22.2%, which represent the actual record of mixed Sn/Pb perovskite solar cells.

Among the various chemical groups that could give an advantage as components of cations, the fluorine atom is of particular interest. In fact, the introduction of molecules containing this chemical group could improve the device's moisture stability.[25] Moreover, the substitution of the hydrogen atoms by the highly electronegative fluorine atoms in organic cations induces a large dipole moment, which increases the polarization in the crystal lattice[26] and may be beneficial for charge carrier separation and transport in solar cells. Fluorinated cations have been implemented in lead (4-fluoro-phenethylammonium iodide)[25,27] and tin perovskite (2-fluoro-phenethylammonium)[28] solar cells. However, a comprehensive analysis of the influence of fluorinated cations on mixed Sn/Pb-perovskites has received limited attention thus far. As only exception, Li and co-workers[29] incorporated a small amount of 2-(4-fluorophenyl)ethylammonium cations in $(MAPbI_3)_{0.75}(FASnI_3)_{0.25}$-based perovskite solar cells, delivering a PCE of 17.51% with a V_{OC} of 0.79 V. The improved device performance was attributed to the formation of a 2D/3D heterostructure that exhibited a preferential alignment perpendicular to the substrate.

In this work, we incorporated a small amount of 2,3,4,5,6-penta-fluorophenethylammonium cations (5FPEAI) in $MA_{0.5}FA_{0.5}Sn_{0.5}Pb_{0.5}I_3$ perovskite, demonstrating an improvement in PCE from 17.47% to 19.13% and in V_{OC} from 0.77 to 0.84 V, when compared to the control devices that do not contain 5FPEAI. The addition of 5FPEAI cations induces superior crystallinity of the 3D perovskite grains and a preferential orientation toward (1 0 0) and (2 0 0) planes while reducing diffraction from the (1 2 0/1 0 2) planes, as confirmed by grazing-incidence wide-angle x-ray scattering (GIWAXS) measurements. The improved ordering of the crystal planes is the leading cause of the enhancement of the perovskite structure's robustness and integrity, which is expected to reduce the amount of tin vacancies and the consequent background carrier density. Furthermore, the highly crystalline films show larger grains and a reduced density of defect states. Finally, the Sn-Pb perovskite solar cell using the fluorinated long organic cation shows much higher thermal stability with respect to the control devices, retaining 90.3% of its initial efficiency after 90 min of thermal stress at 85 °C as compared to 66.2% for the control.

II. RESULTS

In Fig. 1(a), the chemical structure of the 5FPEA cation is shown, which is used in this work as an additive to fabricate solar cells with $MA_{0.5}FA_{0.5}Sn_{0.5}Pb_{0.5}I_3$ as the active layer [Fig. 1(c)], using a planar p-i-n structure with an 0.04 cm^2 active area, as depicted in Fig. 1(b). We introduced the fluorinated molecules in the perovskite structure in an out-of-stoichiometry way, dissolving x mol% of 5FPEAI in the perovskite solution ($5FPEA_xMA_{0.5}FA_{0.5}Sn_{0.5}Pb_{0.5}I_3$). The best control device without 5FPEAI (x = 0) exhibited a PCE of 17.47%, with a V_{OC} of 0.77 V, a short-circuit current (Jsc) of 30.66 mA cm^{-2}, and a fill factor (FF) of 74.19% (see the supplementary material, Table SI). Upon adding 1.25 mol. % of fluorinated molecules, the V_{OC} increases to 0.79 V, bringing the PCE to 18.29%. However, the best device is obtained when using a molar concentration of 1.5% of 5FPEAI. With this composition, a PCE of 19.13%, with a V_{OC} of 0.84 V, a Jsc of 30.93 mA cm^{-2}, and a FF of 73.89% is reached. This PCE is confirmed by
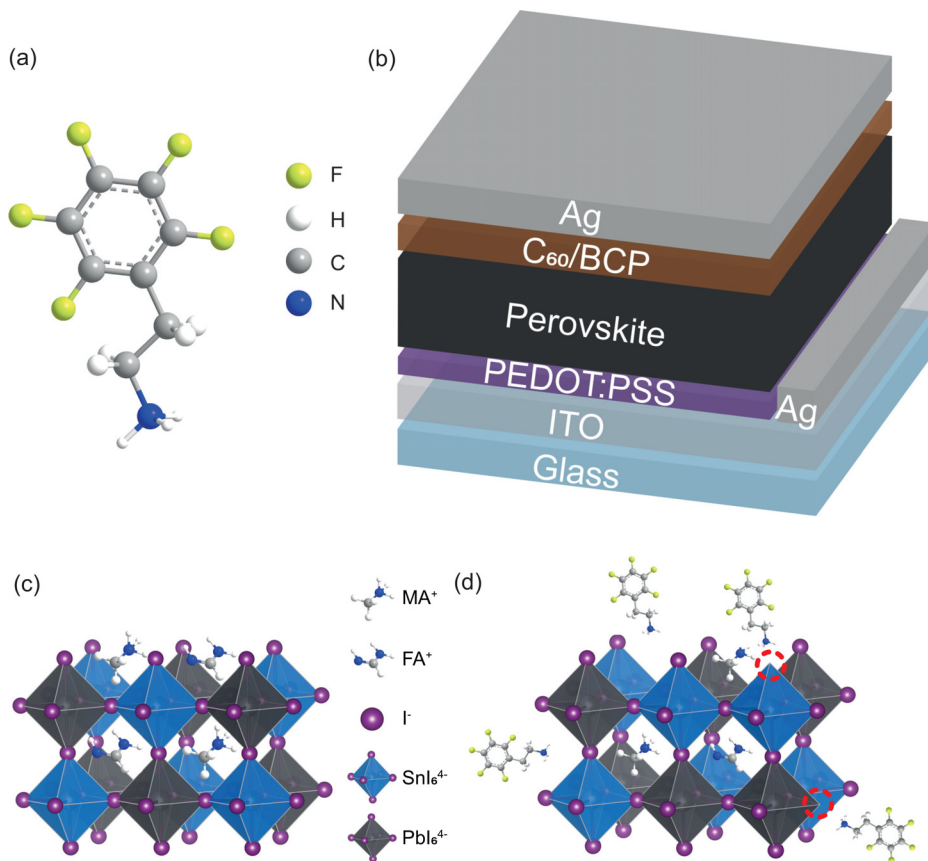
FIG. 1. Schematic representation of (a) the chemical structure of the 5FPEAI molecules, (b) the device structure of the fabricated solar cell PEDOT:PSS = poly(3,4-ethylene dioxythiophene)–poly(styrene sulfonate), BCP = bathocuproine, (c) the crystal structure of $MA_{0.5}FA_{0.5}Sn_{0.5}Pb_{0.5}I_3$ perovskite, and (d) the proposed passivation role of the fluorinated cations.

steady-state measurement, showing a power conversion efficiency of about 18.6% over 100 s (see the supplementary material, Fig. S4). By increasing the concentration further up to 2 mol. %, a decrease in PCE is observed, mainly due to a decreased Jsc from 30.93 to 29.96 mA cm^{-2} and 28.5 mA cm^{-2}, for 1.5, 1.75, and 2 mol. % of 5FPEA, respectively. This is most probably due to the low conductivity of the fluorinated molecule, which at high concentration could act as a barrier for charge transport. For comparison, we also implemented phenethylammonium iodide (PEAI) as additive in the precursor mixture, keeping the same concentration (1.5 mol. %) used for the fluorinated counterpart. In this case, the devices exhibited a V_{OC} of 0.80 V, with a Jsc of 31.22 mA cm^{-2}, a FF of 73.52%, and a PCE of 18.43%. Figure 2(a) shows the J–V curves measured in reverse mode (the forward mode is reported in Fig. S5) of the best devices fabricated with 0 mol. % of 5FPEAI (control), 1.5 mol. % of 5FPEAI, and 1.5 mol. % of PEAI.

From the J–V curves measured under AM1.5 solar spectrum (100 mW cm^{-2} light intensity) illumination, it is evident that the V_{OC} of the mixed Sn/Pb-HP-SCs improves upon the addition of the different organic cations, moving from 0.77 V for the control device to 0.80 and 0.84 V for PEAI and 5FPEAI, respectively. The J–V curves of the three devices in the dark conditions are shown in the inset of Fig. 2(a). The dark current density in reverse bias of the 1.5 mol. % 5FPEAI solar cell is about one order of magnitude lower as compared to the control device. On the contrary, the solar cell using PEAI as additive shows a similar diode behavior and leakage current of the control device.

These results indicate a potential role of 5FPEA and the PEA cations [Fig. 1(d)] in reducing trap-assisted recombination, which leads to an enhanced V_{OC}.

The 5FPEAI-treated and the control devices show a similar EQE spectrum, which gives rise to similar calculated Jsc values for the two solar cells [Fig. 2(b)], namely, 30.33 and 30.55 mA cm^{-2}, for the control and the 5FPEA-treated device, respectively. Both values agree with the short-circuit current as measured from the JV characteristics. The similarity of the EQE spectra is not surprising, as also the UV-vis absorption show identical spectra for the three different compositions [see the supplementary material, Fig. S6(a)], confirming that the inorganic (photoactive) lattice is unaltered and the large organic cations (PEA or 5FPEA) are not incorporated into the perovskite structure. Interestingly, a different color of both modified thin films [with PEAI and 5FPEAI, Fig. S6(b)] is observed right after thermal annealing. This aspect is not fully clarified, because in terms of absorbance, the three films present a similar spectrum. The different hue could be caused by the presence of a wrinkled structure, but this was only observed on the 5FPEAI-based perovskite layers (see the supplementary material, Fig. S7).[30] Further characterization needs to be performed in order to explain this aspect.

The statistical analysis performed on 40 devices is shown in Figs. 3(a)–3(d); in addition to the good reproducibility of the solar cells, we can notice that the average PCE of devices with 1.5 mol. % of 5FPEAI is 18.6% ± 0.2%, which is substantially higher than the
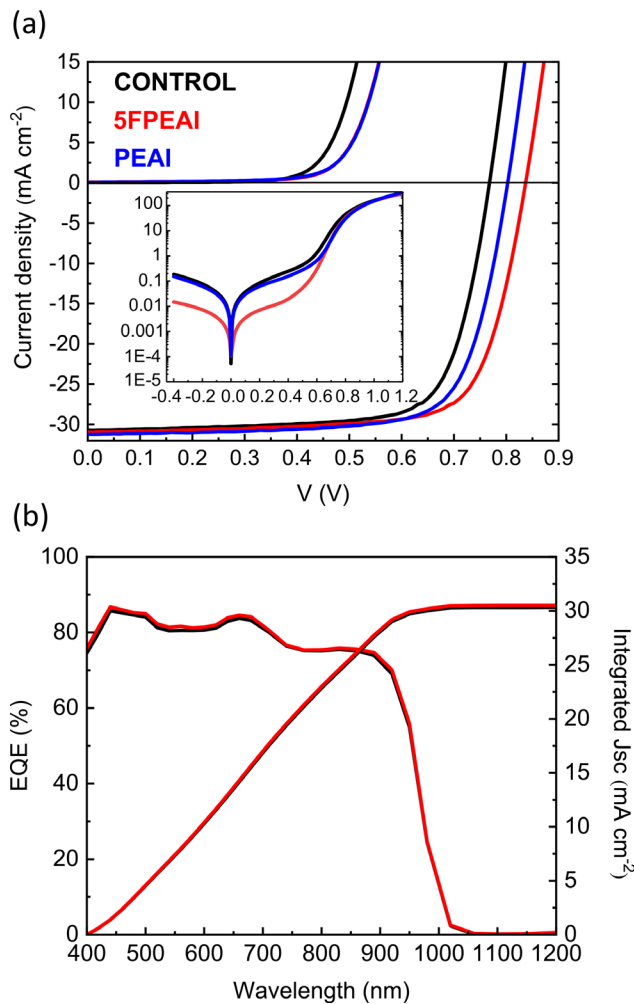
(a)

(b)

FIG. 2. (a) Current density–voltage (J–V) characteristics of perovskite solar cells fabricated with 0 mol. % of 5FPEAI (control, black curve), 1.5 mol. % of PEAI (blue curve), and 1.5 mol. % of 5FPEAI (red curve) measured under AM1.5 solar spectrum (100 mW cm^{-2} light intensity) illumination. The inset graph shows the semi-logarithmic dark J–V curves of the three different devices. (b) External quantum efficiency (EQE) spectra and integrated Jsc of the control device (black curve) and the 5FPEAI-based solar cell (red curve).

average efficiency of the control devices 17.1% $\pm$ 0.3%. The improvement in V_{OC} from 0.76 $\pm$ 0.02 to 0.82 $\pm$ 0.02 V when 5FPEAI is added to the perovskite precursor solution is clearly the main important factor that leads to the increased PCE. Moreover, the statistical analysis exhibits that the 5FPEAI-treated solar cell has a lower Jsc average value, probably due to the insulating nature of the long organic cation.

To understand the reasons behind this significant V_{OC} improvement in 5FPEAI containing device, light intensity-dependent V_{OC} measurements, impedance spectroscopy, and Mott–Schottky analysis were performed on both types of devices (Fig. 4).

In the semilogarithmic plot of the V_{oc} vs light intensity, shown in Fig. 4(a), the 5FPEAI device shows a lower slope with respect to the reference device. The lower slope is an indication of a reduction in

trap-assisted recombination losses.[31] From the dependence of the V_{oc} on the illumination intensity, it is also possible to extract the diode ideality factor through the following expression:

$$V_{OC} \propto n\frac{kT}{q}ln(I), \qquad (1)$$

where k is the Boltzmann constant, T is the temperature in kelvin, q is the elementary charge, I is the light intensity, and n is the ideality factor. The control device displays an ideality factor equal to 1.43, while the 5FPEAI solar cell shows a lower value of 1.17, indicating that bimolecular charge carrier recombination is dominant in the 5FPEAI-based perovskite devices.

From the impedance spectroscopy (Z', Z'') measurements, performed at short-circuit conditions [Fig. 4(b)], we observed a reduction of charge carrier recombination. The charge carrier recombination resistance (R$_4$, see the supplementary material, Fig. S8) in the control device is equal to 258.4 kΩ, which is considerably higher than the value obtained for the 5FPEAI-based device (12.1 kΩ, see the supplementary material, Table SII), indicating that the bulk recombination of the charge carrier is reduced in the treated solar cells.

Using Mott–Schottky analysis [Fig. 4(c)], we measured the variation of the background charge carrier in the two types of devices,

$$C^{-2} = \frac{2}{qA^2\varepsilon_r\varepsilon_0 N_D}\left(V_{bi} + V - \frac{k_B T}{q}\right), \qquad (2)$$

where q is the elementary charge, A is the device geometric area (0.09 cm^2), ε_0 and ε_r are, respectively, the vacuum and relative permittivity, and N$_D$ is the background charge carrier density. The relative permittivity has been calculated using the following equation:

$$\varepsilon_r = \frac{dC}{A\varepsilon_0}, \qquad (3)$$

where d is the thickness of the active layer ($\approx$500 nm) and C is the measured capacitance. The control device showed a background charge carrier density of 1.5×10^{16} cm^{-3}, which is in agreement with the results reported in literature ($1.08 \pm 0.11 \times 10^{16}$),[32,33] while the 5FPEAI-based perovskite solar cell exhibited an almost twofold reduction (7.7×10^{15} cm^{-3}) with respect to the control device. This lower carrier density shows the ability of 5FPEAI to reduce the oxidation of Sn^{2+} and consequently the density of Sn vacancies. We believe that the decreased Sn vacancy density also determines the smaller leakage current observed in the J–V curves measured in the dark conditions [Fig. 2(a)]. Summarizing, the device characterization presented above indicates that 5FPEAI molecules act as a sort of passivating agent that reduce the trap-assisted recombination losses and the Sn vacancies density, resulting mainly in an increased V_{OC}. However, it is not clear how this "sort of passivation agent" works at the microscopic level: is it really a passivation agent that reacts with dangling bonds exposed at the perovskite surface or is the working mechanism more complex?

To answer these questions, we analyzed the XRD diffractograms of the control and passivated films, using both PEAI and 5FPEAI [see the supplementary material, Fig. S9(a)]. All three films exhibit two main diffraction peaks located at 14.1° and 28.4°, which correspond to (1 0 0) and (2 0 0) crystal planes of the cubic 3D (FASnI$_3$)$_{0.5}$(MAPbI$_3$)$_{0.5}$ perovskite structure (see the supplementary material, Table SIII), respectively. The 5FPEAI-based perovskite films
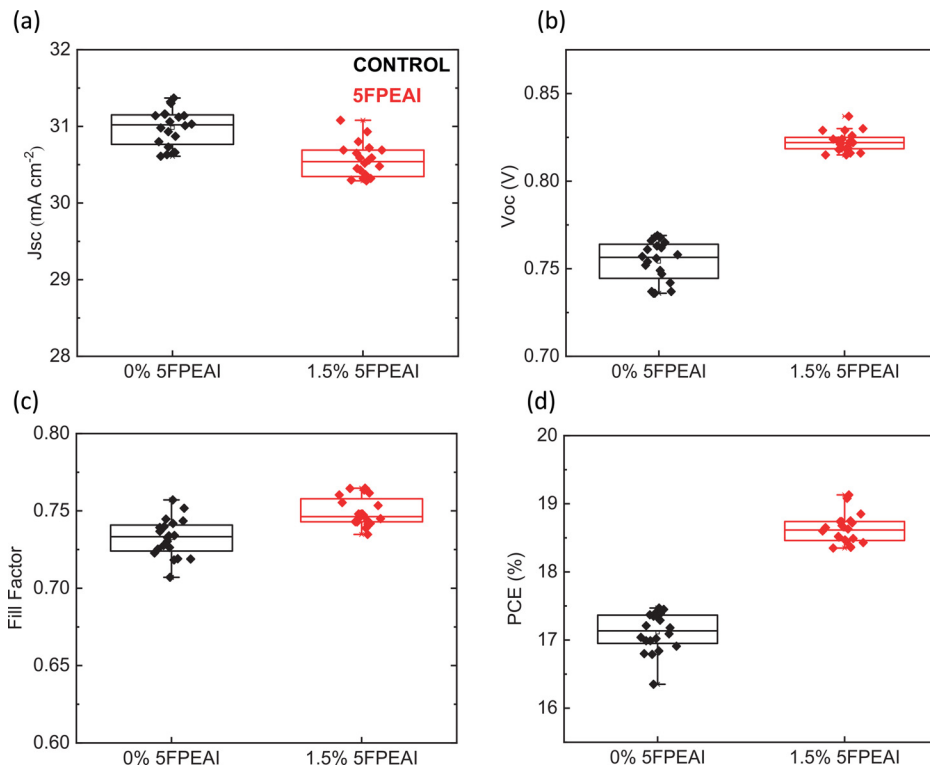
FIG. 3. Statistical distribution of (a) Jsc, (b) V_{OC}, (c) FF, and (d) PCE for 20 devices fabricated with 0 (control, black boxes) and 1.5 mol. % of 5FPEAI (red boxes) molecules.

exhibit higher intensity peaks than the PEAI-based sample and the control film [Fig. S9(b)], demonstrating a higher degree of order. Furthermore, films treated with 5FPEAI display a preferential orientation of the crystalline grains as evidenced by the reduction of the (1 2 0)/(1 0 2) peak located at 24.5° [Fig. S9(c)].

A better understanding of the crystalline structure of the thin films is obtained by angle-resolved GIWAXS measurements (Fig. 5). GIWAXS patterns were taken both close to the film's surface (using a small incident angle of 0.4° providing about 50 nm of penetration inside the films) and in the bulk (using a large incident angle of 2° providing about 350 nm of penetration) of the three deposited films. All the studied films exhibited preferred orientation of the crystallites with their 100 planes oriented parallel to the surface. A minor population of crystallites that have their 111 planes oriented parallel to the substrate are present in all cases (described as 100/111 plane and 200/111 plane in Fig. 5). The control $(FASnI_3)_{0.5}(MAPbI_3)_{0.5}$ film exhibited the lowest degree of orientation with a larger contribution from a Debye–Scherrer isotropic ring centered at $q_z \sim 1.2$ Å that is associated with randomly oriented crystallites. This signal can be seen to be superimposed on the arc-like reflections from the oriented crystallites [Fig. 5(a)]. On the contrary, the modified films, both with PEAI and 5FPEAI, show more pronounced diffraction spots for the {1 0 0}, {0 1 0}, and {1 0 0}/111 plane peaks [Figs. 5(c) and 5(e)], revealing a higher degree of crystallite orientation. A similar trend is detected throughout the bulk of the materials [Figs. 5(b), 5(d), and 5(f)].

The improved order in the treated films can be better visualized when comparing the intensity line cuts along the quasi-vertical q_z direction and the intensity distribution along the azimuthal angle (see the supplementary material, Figs. S10, S11, and S12). We focus the

analysis on the peak intensity and the full-width half maximum (FWHM) of the {1 0 0}, {2 0 0}, {0 1 0}, and {1 0 0}/111 plane peaks. The peak intensity and FWHM are two reliable parameters useful to characterize the perovskite film's degree of order. The {1 0 0}/111 plane peak presents a higher intensity for the 5FPEAI passivated films with respect to the PEA-treated and control compounds in both the surface and bulk of the material, as shown by the GIWAXS intensity line cuts along the quasi-vertical q_z direction [see the supplementary material, Figs. S10(a), and S10(b)]. The angular profiles further underline the enhanced intensity of both {1 0 0} peaks with (100) and (111) planes parallel to the substrates [Figs. S11(a), and S11(b)]. Moreover, Fig. S11(a) clearly shows the reduced contribution of the Debye–Scherrer ring located at $q_z = 1.2$ Å, indicating a reduction of randomly oriented crystallites in the treated films. The higher peak intensity for the PEAI and 5FPEAI films is evident after normalization of the angular profiles at $q_z \approx 1$ Å and $q_r \approx 0.5$ Å [see the supplementary material, Fig. S11(b)]. A similar trend could be also observed for the other signals present in the GIWAXS pattern.

To determine the FWHM of the different peaks, we performed a fit of the intensity profiles alongside the azimuthal χ-angle for the GIWAXS data collected for the bulk of the films (see the supplementary material, Fig. S12). The diffraction spots in Fig. S12 can be fitted using Gaussian functions as follows:

$$y = \frac{A \, e^{\frac{-4\ln(2)(x-x_C)^2}{w^2}}}{w\sqrt{\frac{\pi}{4\ln(2)}}}, \tag{4}$$
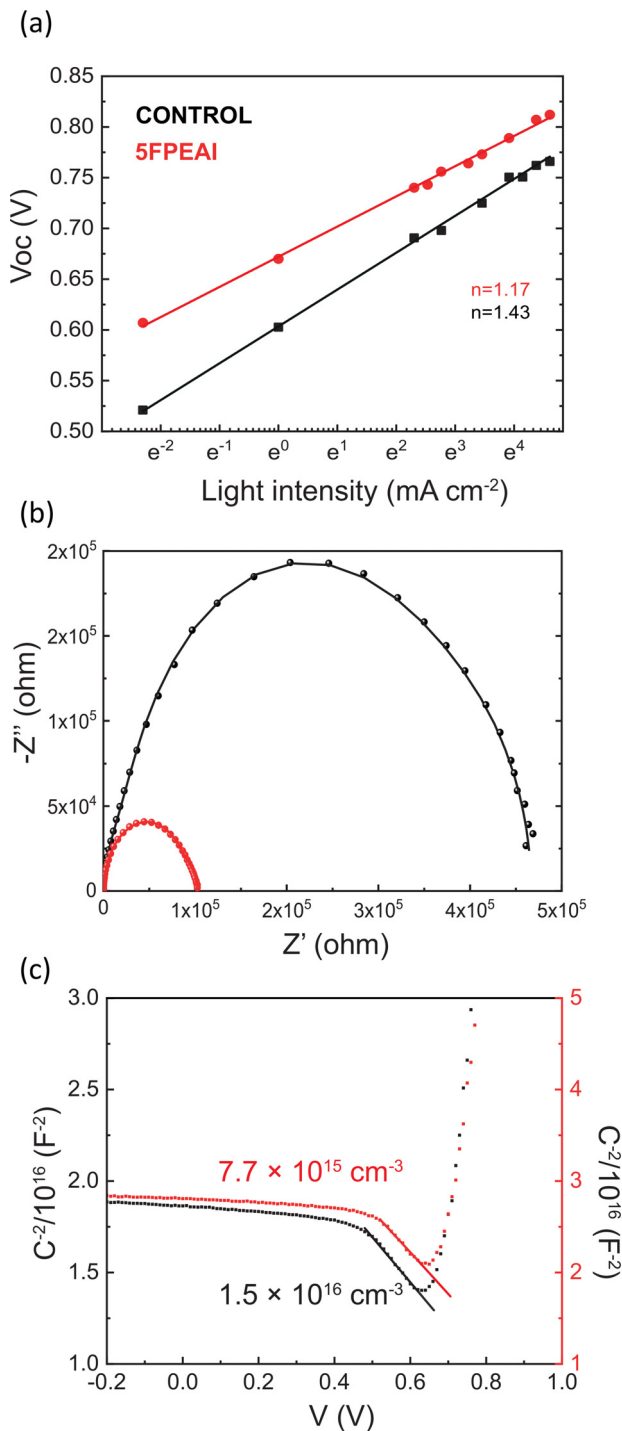
FIG. 4. (a) Light intensity vs V_{OC} measurements of the control (black curve) and 1.5 mol. % 5FPEAI devices (red curve). (b) Impedance spectra recorded in the dark and at short-circuit conditions of both control (black curve) and treated (red curve) solar cells. The continuous line represents the fitting, while the dots are the experimental data. (c) C^{-2} vs applied voltage of the devices fabricated without (black curve) and with (red curve) 1.5 mol. % of 5FPEAI molecules. Measurements were performed in the dark conditions.

where x_c is the center of the Gaussian, A is the area, and w is the FWHM of the function. The FWHM for the {1 0 0} peak is reduced upon the addition of the larger cations, going from 14 for the control films to 12 and 11.9 for the PEAI and 5FPEAI-treated films, respectively. A similar trend was observed for the {1 0 0}/111 plane peak (see the supplementary material, Table SIV). Finally, the GIWAXS images revealed no presence of any signal located at low q_z values around $0.5\,\text{Å}^{-1}$ that would be associated with low-dimensional 2D structures.[34,35] These signals were detected neither on the surface nor in the bulk of the passivated films (PEAI or 5FPEAI) [see the supplementary material, Figs. S10(c) and S10(d)]. Two possible explanations could be formulated here: first, the low quantity of bulky cations could create a limited amount of low-dimensional perovskite, that is, difficult to detect by x-ray diffraction techniques; second, PEAI or 5FPEAI molecules are improving the film crystallinity without creating a 2D structure due to the low concentration with respect to the other ions in the perovskite structure. Since it is well known that tethering ammonium cations prefer to distribute themselves along the grain boundaries and at the interface with substrates,[10,36,37] the second hypothesis seems more likely to be true.[38]

To clarify which is the right scenario, we fabricated films with higher 5FPEAI and PEAI concentration (20 mol. %). The XRD analysis performed on these films revealed the presence of four peaks assigned to (020), (040), (060), and (080) planes [see the supplementary material, Figs. S13(a)–S13(c)]. These additional peaks have been assigned to the presence of lower dimensional perovskite phase,[39] revealing that when the cations concentration is 1.5 mol. % 5FPEAI and PEAI only improve the crystallinity.

Summarizing, we can conclude that the bulky organic cations help the crystal lattice to orient preferentially along the *h00* direction, improving the order of the $(FASnI_3)_{0.5}(MAPbI_3)_{0.5}$ material.

After having obtained a deep understanding of the crystallinity of the samples, now the surface is left for our SEM investigation (Fig. 6). The control film showed a compact morphology with few pinholes and well-defined grain boundaries [Fig. 6(a), see the supplementary material Figs. S14(c) and S14(d)]. Likewise, the FPEAI film shows good surface coverage and exhibits similar grain sizes (see also AFM in Fig. S15). Previous studies proposed that structural defects such as dangling bonds or vacancies preferably form at the grain boundaries rather than in the bulk.[31,40,41] Therefore, non-radiative recombination mainly occurs at the grain boundaries. The addition of a small amount of 5FPEAI fuses the grains together and seems to blur the grain boundaries [Figs. 6(b) and 6(c)]. The higher magnification SEM images on both control and 5FPEAI-based perovskite films [Figs. 6(c), 6(d), S14(c), and S14(d)] clearly show the fused grains and the wrinkled structure present in the 5FPEAI-based perovskite films. Moreover, the 5FPEAI films present fewer pinholes with respect to the control films. Figures S14(a) and S14(b) show the SEM images of PEAI-treated perovskite films for comparison. Similar to the 5FPEAI-treated films, also these samples showed lower pinhole formation, but the grain fusion is less evident than in the case of the samples treated with the fluorinated derivatives. Obviously, both the decreased number of pinholes and the fused grain boundaries are characteristics that are very beneficial for the device's scalability and performance. Moreover, the surface roughness is reduced going from 29.39 to 21.69 nm for the control and 5FPEAI passivated films, respectively (Fig. S15 and the supplementary material, Table SV). This decreased surface roughness
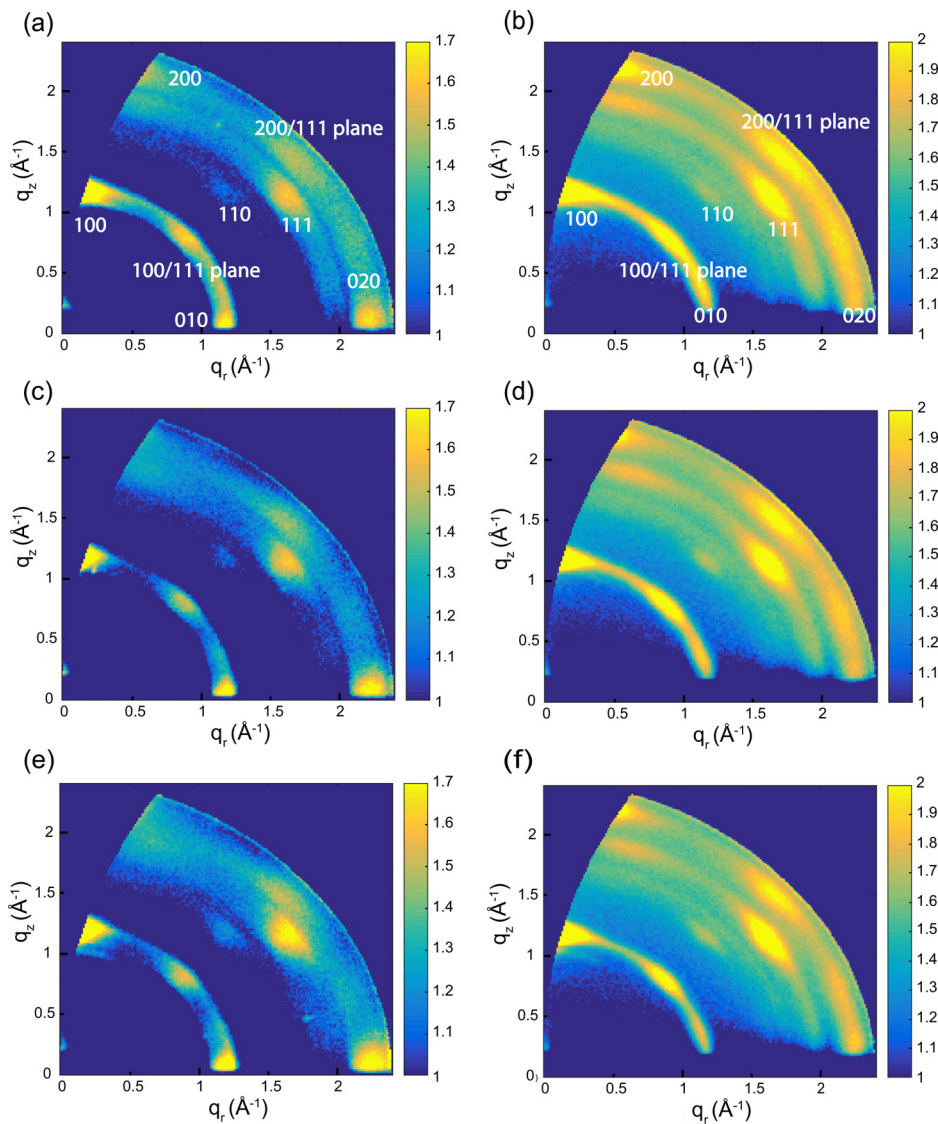
FIG. 5. GIWAXS images of the films deposited on a PEDOT:PSS layer recorded at an incident angle of 0.4°: (a) $(FASnI_3)_{0.5}(MAPbI_3)_{0.5}$, (c) $PEA_{0.015}(FASnI_3)_{0.5}(MAPbI_3)_{0.5}$, and (e) $5FPEA_{0.015}(FASnI_3)_{0.5}(MAPbI_3)_{0.5}$. GIWAXS of the same films recorded at 2° as incident angle: (b) control, (d) PEA-, and (f) 5FPEA-treated perovskite films.

might also play a role in the different visual appearance of the films when seen by the naked eye.

To verify our assumption on the scalability of the solar cells, we fabricated devices with active area of 0.04, 0.09, 0.25, and 0.80 cm². Figure S16 shows the J–V characteristics of the best control and 5FPEA passivated devices. All the parameters are summarized in Table SVI. When the active area increases, both devices exhibit a decrease in efficiency mainly due to a reduction in FF and Jsc. A higher series resistance causes this reduction. The control device with an active area of 0.8 cm² showed a PCE of only 7.48%, which constitutes a relative loss of 56.54% with respect to the 0.04 cm² active area device. The 5FPEAI-treated device, on the other hand, shows an efficiency of 10.88%, which is only a 43.12% decrease with respect to the 0.04 cm² device. This is indeed what we expected, considering the reduced density of pinholes and surface defects. For the FF, the dependence on the

active area is also strong; in the case of the 5FPEAI perovskite, the FF goes from 73.89% to 50.15% when the area scales from 0.04 to 0.80 cm². On the contrary, the control device showed a FF reduction from 73.68% to a mere 39.51%. The considerably higher FF of the 5FPEAI 0.8 cm² perovskite solar cells with respect to the control device is due to the lower series resistance in the former (14.78 and 17.83 Ω cm² for passivated and control devices, respectively).

Finally, after all the material and device characterization described above, we can answer to the previously formulated questions on the role of 5FPEAI molecules in the perovskite system. Essentially, an improved crystallinity and a lower trap state density have been observed for the treated films. We believe that during the perovskite film formation from the precursor solution, the fluorinated molecules migrate to the solution/air and solution/substrate interfaces. Here, the few 5FPEAI molecules present in the system coordinate to the
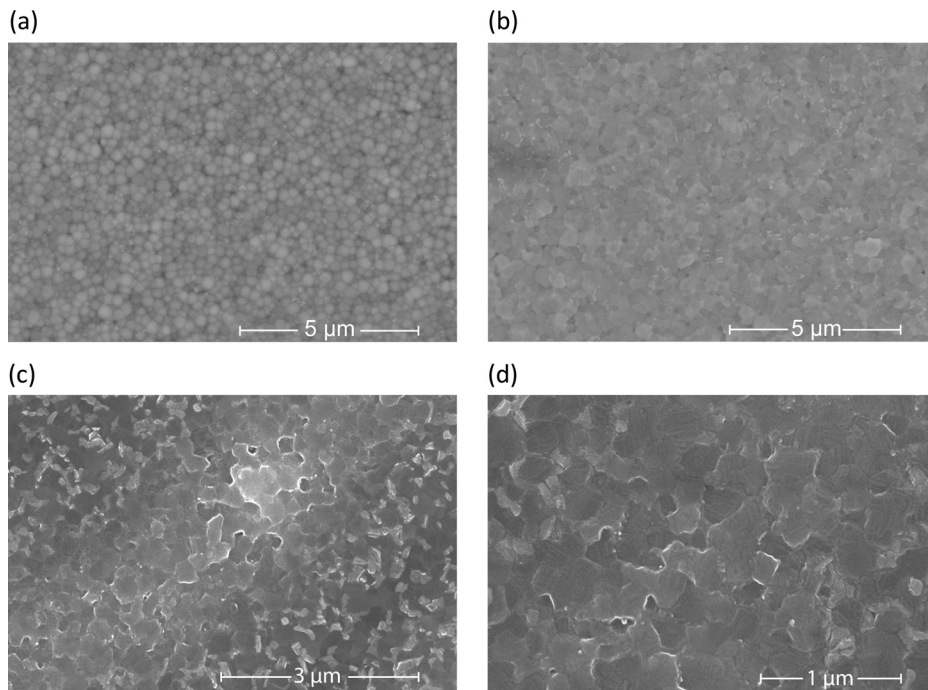
FIG. 6. SEM images on (a) control sample and (b) 5FPEAI-based perovskite films. Higher magnification SEM images, 3 μm (c) and 1 μm scale (d) on the 5FPEAI$_{0.015}$MA$_{0.5}$FA$_{0.5}$Sn$_{0.5}$Pb$_{0.5}$I$_3$ film. All the films have been deposited on an ITO/PEDOT:PSS substrates.

periphery of Sn/Pb halide octahedra and later to the edges of the growing crystals, forcing a better alignment of the crystals with the (100) plane-parallel to the substrates. This behavior has been reported previously in tin halide perovskite with the use of PEAI molecules.[37] The presence of 5FPEAI molecules on the surface could also help to reduce the A$^+$/I$^-$ vacancies located at the perovskite surface. Moreover, the different morphology analyzed through the SEM could be an indication of an altered crystallization of the 5FPEAI-treated films and, a potential presence of the 5FPEA$^+$ cations at the surface.

An important objective for perovskite solar cells is to improve their long-term thermal and environment stability. Figures 7(a) and 7(b) show the stability of our devices in a N$_2$ atmosphere and under thermal stress at 85 °C, respectively. The unencapsulated 5FPEA-based solar cell exhibits better long-term stability with respect to the control unencapsulated device, retaining 86.5% of its initial efficiency after being stored in

a N$_2$ atmosphere (O$_2$ < 0.1 ppm, H$_2$O < 0.1 ppm) for 28 days. Under the same condition, the control device drops from initial PCE down to 74.6%. The improved stability in N$_2$ is attributed to the reduction in grain boundaries and surface defect density in the 5FPEA-based device. Several previous studies have reported that the fast device degradation can be directly correlated with the grain boundaries; interestingly, this is also happening in the absence of oxygen (*vide infra*).[42,43]

The 5FPEAI-treated device displays a small drop (9.7%) of its initial PCE after 90 min of continuous thermal annealing, while the control device exhibited a 33.7% loss of its initial efficiency. It is generally believed that the thermal instability of these materials is due to the evaporation of small organic cations, mostly from the grain boundaries.[44] The 5FPEAI-treated sample has a lower number of these weak regions from which loss of the organic cation can take place. Furthermore, it is also possible that the presence of the longer organic
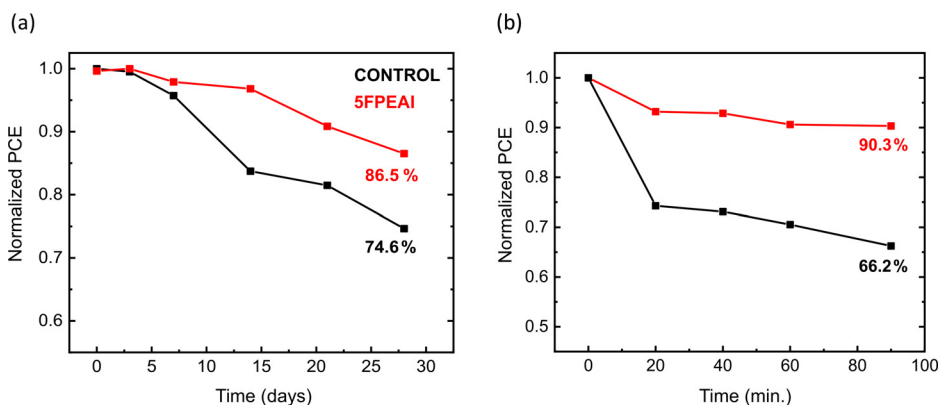

FIG. 7. (a) Stability test of the control (black curves) and 5FPEAI-based (red curves) perovskite solar cell stored in a N$_2$ inert atmosphere at room temperature (25 °C). (b) Stability test of the same devices under thermal stress at 85 °C in a N$_2$ inert atmosphere.

molecule as passivating agent on the surface hinders the desorption of the small organic cation. Experiments on thermal stress of the PEA-based perovskite solar cells (see the supplementary material, Fig. S17) show that this composition maintains only 74.3% of its initial efficiency, while this is 90.3% for the 5FPEA-based devices. These results again underline the important role of the fluorination of the cation in improving the performance and stability of perovskite solar cells.

A further testament to the improved material stability of the passivated samples is found in their respective photoluminescence spectra (see the supplementary material, Fig. S18). Aside from the main emission peak of $(FASnI_3)_{0.5}(MAPbI_3)_{0.5}$ around 975 nm, an additional high-energy emission feature was found to develop in the range 700–750 nm range upon exposure of the sample to a pulsed 400 nm laser (50 μW, 76 MHz) in N_2. This feature is particularly pronounced for the control film, both on quartz as well as on PEDOT: PSS, whereas it is only present for the PEA film on PEDOT:PSS and not observable at all in the case of 5FPEA. The emergence of this high-energy peak upon photo-excitation points to material decomposition that is effectively suppressed when 5FPEA cations are introduced into the system. We would also like to highlight at this point that no high-energy emission from low-dimensional perovskite phases could be observed in the photoluminescence spectra of the PEA and 5FPEA films, confirming that the small quantity of these cations does not allow to form low-dimensional phases.

Finally, to understand how these photo-induced changes would impact device stability, we traced the PL intensity of the perovskite films cast on PEDOT:PSS over time (see the supplementary material, Fig. S19). At t = 0, right after unblocking the laser, the PL intensity from the control film is higher than that of the PEA and 5FPEA films owing to the efficient charge extraction in the latter. Interestingly, while the control film shows a continuous decrease in PL intensity owing to photo-induced degradation, the two long cations samples exhibit distinctly different behavior. Both the PEA and 5FPEA show an initial increase in their PL intensity, which we interpret as a photo-healing effect as we have previously reported for several different perovskites.[45–47] This initial photo-healing is followed by a continuous degradation as observed for the control sample. It is interesting to point out that while the magnitude of the healing effect is larger for the 5FPEA film than for the PEA film, both materials show a qualitatively similar response to prolonged light exposure.

III. CONCLUSIONS

In conclusion, we demonstrated that the use of 2,3,4,5,6-pentafluorophenethylammonium cations in $(FASnI_3)_{0.5}(MAPbI_3)_{0.5}$ perovskite substantially improves the V_{OC} of solar cells. The champion device shows a V_{OC} of 0.84 V and a PCE of 19.13%. The addition of a small amount of 5FPEA cations gives rise to the homogenous growth of crystalline and well-oriented perovskite grains. The enhanced crystallinity and the fused grains appear as the main reason for the reduction of the number of grain boundaries, the lower background carrier density, and the decreased trap-assisted recombination losses with respect to the control devices. In addition, the improved crystallinity of the perovskite layer alongside the reduced trap state density on the perovskite surface caused by the addition of 5FPEA cations reduces the photo-induced degradation and enhances the device's thermal stability. As expected, the improved quality of the film is fundamental to improve the device scalability, with 57% and 43% loss in efficiency

when scaling the active area from 0.04 to 0.8 cm^2, for the control and 5FPEA-based device, respectively. We believe that these results will open the way toward a more intense investigation of the use of fluorinated molecules in Pb/Sn perovskite solar cells, which have the potential to surpass the efficiency of Pb-based perovskite devices.

IV. EXPERIMENTAL METHODS
A. Fabrication of PSCs

ITO glasses (30×30 mm^2) were washed using soapy water and subsequently sonicated in de-ionized water, acetone, and isopropyl alcohol (IPA). The ITO glasses were then dried in air at 130 °C for 10 min to remove the excess IPA. After drying, the ITO-coated glasses were treated with UV-Ozone for 30 min. A PEDOT:PSS layer was then spin-coated at 3000 rpm for 60 s and annealed at 140 °C for 20 min. The final solutions were prepared by mixing the $MAPbI_3$ solution with the $FASnI_3$ (1:1 molar ratio) solution in a N_2-filled glovebox. The $MAPbI_3$ solution was prepared by dissolving 1.4 mmol of PbI_2, 1.4 mmol of MAI, and 0.048 95 mmol of $Pb(SCN)_2$ in 0.9 ml of dimethylformamide (DMF) and 0.1 ml of dimethyl sulfoxide (DMSO) (DMF:DMSO = 9:1). The $FASnI_3$ was prepared by dissolving 1.4 mmol of FAI, 1.4 mmol of SnI_2, and 0.14 mmol of SnF_2 in 0.8 ml of DMF and 0.2 ml of DMSO (DMF:DMSO = 4:1). In the final $MA_{0.5}FA_{0.5}Pb_{0.5}Sn_{0.5}I_3$ (1.4 M) solution was added 0.021 M of 5FPEAI or PEAI to realize $5FPEAI_{0.015}MA_{0.5}FA_{0.5}Pb_{0.5}Sn_{0.5}I_3$ and $PEA_{0.015}MA_{0.5}FA_{0.5}Pb_{0.5}Sn_{0.5}I_3$, respectively. The filtered solutions (80 μl for each substrate) were spin-coated at 4000 rpm for 60 s in a N_2-filled glovebox with O_2 and H_2O concentration of <0.1 ppm. 0.5 ml of diethyl ether was dropped 15 s after the start of the spinning process. After preparation, perovskite films were immediately annealed at 100 °C for 10 min on a hotplate. Then, the samples were transferred to a vacuum chamber where 60 nm of C_{60} and 6 nm of BCP were evaporated at 5×10^{-7} mbar. Finally, 100 nm of Ag was evaporated on top of BCP layer under a pressure of 10^{-8} mbar.

B. Characterization
1. J–V characteristics

The J–V curves of the perovskite solar cells were measured in a N_2 filled glovebox ($O_2 < 0.1$ ppm and $H_2O < 0.1$ ppm). The standard test conditions (295 K, AM 1.5 G solar illumination) have been applied to measure all devices using a Keithley 2400 source meter and a Steuernagel Solar constant 1200 metal halide lamp. The light intensity was calibrated by using a Si reference cell. A shadow mask (0.04, 0.09, 0.25, and 0.8 cm^2) was used to exclude lateral contributions beyond the device area.

2. EQE measurements

A home-build setup was used to measure the external quantum efficiency (EQE) of the fabricated solar cells. In our setup, a xenon lamp is used as light source, which is guided through three filter wheels to cover a spectral range from 400 to 1400 nm. The wavelength interval is of 20 nm and 30 nm for values smaller and bigger than 680 nm, respectively. After the filter wheels, the light is chopped and focused on the sample. All the measurements are performed in nitrogen atmosphere. The obtained photocurrent is measured using a lock-in amplifier (Stanford Research Systems, Model SR830 DSP lock-in amplifier). For the calibration of the photon flux, a set of Newport optical power

detectors (Newport Model 818-SL and Model 818-IR) have been used. Finally, the integrated Jsc value is multiplied by the calculated mismatch factor value (1.07) due to the slightly different spectral responses of the perovskite and the silicon solar cells used to calibrate the setup.

3. Impedance measurements

The capacitance–voltage (C–V) measurements are performed using a Solarton 1260 impedance gain-phase analyzer. Specifically, we carried out the measurement under dark conditions, applying a AC drive voltage with a frequency of 10 kHz and an amplitude of 10 mV, while the applied DC bias is swapped in the range of −0.2 to 1 V. The C–f measurements are performed using a SP-200 bio-logic potentiostat equipped with an electrochemical impedance spectroscopy analyzer. An ac voltage, with a 10 mV amplitude, is applied at zero voltage (short-circuit condition) under 1 sun illumination.

4. GIWAXS measurements

GIWAXS measurements are carried out using a MINA x-ray scattering instrument with a Cu rotating anode source ($\lambda = 1.5413$ Å). To collect all the different patterns, a Vantec500 detector (1024×1024 pixel array with pixel size $136 \times 136 \, \mu m$) placed 93 mm away from the films. The perovskite films are placed in reflection geometry at certain incident angles α_i with respect to the direct beam using a Huber goniometer. The α_i angles are set to $0.4°$ and $2.0°$ to probe the thin film structure at the surface (50 nm) and inside (350 nm) the layer. For the calculation, the densities of $3.95 \, g \, cm^{-3}$ is used for all the perovskite compounds.[48] A silicon substrate with native oxide on top has been used to calibrate the direct beam center position on the detector and the sample-to-detector distance. GIXGUI Matlab toolbox has been implemented to analyze and correct the GIWAXS geometry of the raw pattern.[49]

5. SEM measurements

SEM images were recorded using a NovaNano SEM 650 with an acceleration voltage of 18 kV.

6. XRD measurements

XRD patterns of the three different perovskite films (Fig. S9) were recorded in air without any encapsulation (moisture about 20%, temperature about 20 °C) on a Bruker D8 Advance x-ray diffractometer with a Cu Kα source ($\lambda = 1.54$ Å) and a Lynxeye detector.

7. UV-vis measurements

A Shimatzu UV-Vis-NIR spectrophotometer (UV 3600) was used to record the UV-vis spectra of the fabricated films without encapsulation.

8. AFM measurements

A Bruker Multimode eight microscope with ScanAsyst air probes (resonant frequency 70 kHz, spring constant 0.4 N m^{-1}) was used to investigated the perovskite film morphology in air. Micrographs were recorded using a scan rate of 0.912 Hz with a resolution of 512 samples

per line. The data were later analyzed with Gwyddion–free scanning probe microscope (SPM) [AFM, scanning near-field optical microscope (SNOM)/near-field scanning optical microscopy (NSOM), scanning tunneling microscopy (STM), magnetic force microscopy (MFM), …] data analysis software.

9. PL measurements

PL measurements were obtained by exciting the sample with the second harmonic (400 nm) of a mode-locked Ti:sapphire laser (Mira900, coherent) operating at a repetition rate of 76 MHz. The beam profile was spatially restricted by passing it through an iris, after which the beam power was modulated by an adjustable neutral density filter. The photoluminescence was collected and dispersed by a monochromator with a 50 lines mm^{-1} grating. The dispersed spectrum was subsequently captured using a Hamamatsu image CCD (ImageEM).

SUPPLEMENTARY MATERIAL

See the supplementary material for captions of supporting Figs. S1–S19 and for Tables SI–SVI.

AUTHOR DECLARATIONS
Conflict of Interest

The authors have no conflicts to disclose.

DATA AVAILABILITY

The data that support the findings of this study are available within the article and its supplementary material.

REFERENCES

[1]J. M. Ball, S. D. Stranks, M. T. Hörantner, S. Hüttner, W. Zhang, E. J. W. Crossland, I. Ramirez, M. Riede, M. B. Johnston, R. H. Friend, and H. J. Snaith, "Optical properties and limiting photocurrent of thin-film perovskite solar cells," Energy Environ. Sci. **8**, 602 (2015).

[2]F. Zhang, B. Yang, Y. Li, W. Deng, and R. He, "Extra long electron–hole diffusion lengths in $CH_3NH_3PbI_{3−x}Cl_x$ perovskite single crystals," J. Mater. Chem. C **5**, 8431 (2017).

[3]M. Baranowski and P. Plochocka, "Excitons in metal-halide perovskites," Adv. Energy Mater. **10**, 1903659 (2020).

[4]L. M. Herz, "Charge-carrier mobilities in metal halide perovskites: Fundamental mechanisms and limits," ACS Energy Lett. **2**, 1539 (2017).

[5]H. Min, D. Y. Lee, J. Kim, G. Kim, K. S. Lee, J. Kim, M. J. Paik, Y. K. Kim, K. S. Kim, M. G. Kim, T. J. Shin, and S. Il Seok, "Perovskite solar cells with atomically coherent interlayers on SnO$_2$ electrodes," Nature **598**, 444 (2021).

[6]K. Yoshikawa, H. Kawasaki, W. Yoshida, T. Irie, K. Konishi, K. Nakano, T. Uto, D. Adachi, M. Kanematsu, H. Uzu, and K. Yamamoto, "Silicon

heterojunction solar cell with interdigitated back contacts for a photoconversion efficiency over 26%," Nat. Energy **2**, 17032 (2017).

[7] A. Babayigit, A. Ethirajan, M. Muller, and B. Conings, "Toxicity of organometal halide perovskite solar cells," Nat. Mater. **15**, 247 (2016).

[8] X. Jiang, Z. Zang, Y. Zhou, H. Li, Q. Wei, and Z. Ning, "Tin halide perovskite solar cells: An emerging thin-film photovoltaic technology," Acc. Mater. Res. **2**, 210 (2021).

[9] D. Meggiolaro, D. Ricciarelli, A. A. Alasmari, F. A. S. Alasmary, and F. De Angelis, "Tin versus lead redox chemistry modulates charge trapping and self-doping in tin/lead iodide perovskites," J. Phys. Chem. Lett. **11**, 3546 (2020).

[10] S. Shao, J. Liu, G. Portale, H. H. Fang, G. R. Blake, G. H. ten Brink, L. J. A. Koster, and M. A. Loi, "Highly reproducible Sn-based hybrid perovskite solar cells with 9% efficiency," Adv. Energy Mater. **8**, 1702019 (2018).

[11] B. Bin Yu, Z. Chen, Y. Zhu, Y. Wang, B. Han, G. Chen, X. Zhang, Z. Du, and Z. He, "Heterogeneous 2D/3D tin-halides perovskite solar cells with certified conversion efficiency breaking 14%," Adv. Mater. **33**, 2102055 (2021).

[12] A. Amat, E. Mosconi, E. Ronca, C. Quarti, P. Umari, M. Nazeeruddin, M. Gra, and F. De Angelis, "Cation-induced band-gap tuning in organohalide perovskites: Interplay of spin–orbit coupling and octahedra tilting," Nano Lett. **14**, 3608 (2014).

[13] Y. Ogomi, A. Morita, S. Tsukamoto, T. Saitho, N. Fujikawa, Q. Shen, T. Toyoda, K. Yoshino, S. S. Pandey, and S. Hayase, "CH$_3$NH$_3$Sn$_x$Pb$_{(1-x)}$I$_3$ perovskite solar cells covering up to 1060 nm," J. Phys. Chem. Lett. **5**, 1004 (2014).

[14] R. Lin, K. Xiao, Z. Qin, Q. Han, C. Zhang, M. Wei, M. I. Saidaminov, Y. Gao, J. Xu, M. Xiao, A. Li, J. Zhu, E. H. Sargent, and H. Tan, "Monolithic all-perovskite tandem solar cells with 24.8% efficiency exploiting comproportionation to suppress Sn(II) oxidation in precursor ink," Nat. Energy **4**, 864 (2019).

[15] T. Supasai, N. Rujisamphan, K. Ullrich, A. Chemseddine, and T. Dittrich, "Formation of a passivating CH$_3$NH$_3$PbI$_3$/PbI$_2$ interface during moderate heating of CH$_3$NH$_3$PbI$_3$ layers," Appl. Phys. Lett. **103**, 183906 (2013).

[16] C. C. Stoumpos, C. D. Malliakas, and M. G. Kanatzidis, "Semiconducting tin and lead iodide perovskites with organic cations: Phase transitions, high mobilities, and near-infrared photoluminescent properties," Inorg. Chem. **52**, 9019 (2013).

[17] N. K. Noel, S. D. Stranks, A. Abate, C. Wehrenfennig, S. Guarnera, A. A. Haghighirad, A. Sadhanala, G. E. Eperon, S. K. Pathak, M. B. Johnston, A. Petrozza, L. M. Herz, and H. J. Snaith, "Lead-free organic–inorganic tin halide perovskites for photovoltaic applications," Energy Environ. Sci. **7**, 3061 (2014).

[18] G. Kapil, T. Bessho, T. Maekawa, A. K. Baranwal, Y. Zhang, M. A. Kamarudin, D. Hirotani, Q. Shen, H. Segawa, and S. Hayase, "Tin-lead perovskite fabricated via ethylenediamine interlayer guides to the solar cell efficiency of 21.74%," Adv. Energy Mater. **11**, 2101069 (2021).

[19] M. Jeong, I. W. Choi, E. M. Go, Y. Cho, M. Kim, B. Lee, S. Jeong, Y. Jo, H. W. Choi, J. Lee, J. H. Bae, S. K. Kwak, D. S. Kim, and C. Yang, "Stable perovskite solar cells with efficiency exceeding 24.8% and 0.3-V voltage loss," Science **369**, 1615 (2020).

[20] J. Tong, Z. Song, D. H. Kim, X. Chen, C. Chen, A. F. Palmstrom, P. F. Ndione, M. O. Reese, S. P. Dunfield, O. G. Reid, J. Liu, F. Zhang, S. P. Harvey, Z. Li, S. T. Christensen, G. Teeter, D. Zhao, M. M. Al-Jassim, M. Van Hest, M. C. Beard, S. E. Shaheen, J. J. Berry, Y. Yan, and K. Zhu, "Carrier lifetimes of >1 μs in Sn-Pb perovskites enable efficient all-perovskite tandem solar cells," Science **364**, 475 (2019).

[21] K. Xiao, R. Lin, Q. Han, Y. Hou, Z. Qin, H. T. Nguyen, J. Wen, M. Wei, V. Yeddu, M. I. Saidaminov, Y. Gao, Y. Luo, Y. Wang, H. Gao, C. Zhang, J. Xu, J. Zhu, E. H. Sargent, and H. Tan, "All-perovskite tandem solar cells with 24.2% certified efficiency and area over 1 cm^2 using surface-anchoring zwitterionic antioxidant," Nat. Energy **5**, 870 (2020).

[22] M. Wei, K. Xiao, G. Walters, R. Lin, Y. Zhao, M. I. Saidaminov, P. Todorović, A. Johnston, Z. Huang, H. Chen, A. Li, J. Zhu, Z. Yang, Y. K. Wang, A. H. Proppe, S. O. Kelley, Y. Hou, O. Voznyy, H. Tan, and E. H. Sargent, "Combining efficiency and stability in mixed tin–lead perovskite solar cells by capping grains with an ultrathin 2D layer," Adv. Mater. **32**, 1907058 (2020).

[23] W. Ke, C. Chen, I. Spanopoulos, L. Mao, I. Hadar, X. Li, J. M. Hoffman, Z. Song, Y. Yan, and M. G. Kanatzidis, "Narrow-bandgap mixed lead/tin-based 2D Dion-Jacobson perovskites boost the performance of solar cells," J. Am. Chem. Soc. **142**, 15049 (2020).

[24] R. Lin, J. Xu, M. Wei, Y. Wang, Z. Qin, Z. Liu, J. Wu, K. Xiao, B. Chen, S. M. Park, G. Chen, H. R. Atapattu, K. R. Graham, J. Xu, J. Zhu, L. Li, C. Zhang, E. H. Sargent, and H. Tan, "All-perovskite tandem solar cells with improved grain surface passivation," Nature **603**, 73–78 (2022).

[25] H. B. Lee, N. Kumar, B. Tyagi, K. J. Ko, and J. W. Kang, "Dimensionality and defect engineering using fluoroaromatic cations for efficiency and stability enhancement in 3D/2D perovskite photovoltaics," Sol. RRL **5**, 2000589 (2021).

[26] P. P. Shi, S. Q. Lu, X. J. Song, X. G. Chen, W. Q. Liao, P. F. Li, Y. Y. Tang, and R. G. Xiong, "Two-dimensional organic-inorganic perovskite ferroelectric semiconductors with fluorinated aromatic spacers," J. Am. Chem. Soc. **141**, 18334 (2019).

[27] R. Guo, A. Buyruk, X. Jiang, W. Chen, L. K. Reb, M. A. Scheel, T. Ameri, and P. Müller-Buschbaum, "Tailoring the orientation of perovskite crystals via adding two-dimensional polymorphs for perovskite solar cells," J. Phys. Energy **2**, 034005 (2020).

[28] E. Jokar, P. Y. Cheng, C. Y. Lin, S. Narra, S. Shahbazi, and E. Wei-Guang Diau, "Enhanced performance and stability of 3D/2D tin perovskite solar cells fabricated with a sequential solution deposition," ACS Energy Lett. **6**, 485 (2021).

[29] C. Li, Y. Pan, J. Hu, S. Qiu, C. Zhang, Y. Yang, S. Chen, X. Liu, C. J. Brabec, M. K. Nazeeruddin, Y. Mai, and F. Guo, "Vertically aligned 2D/3D Pb–Sn perovskites with enhanced charge extraction and suppressed phase segregation for efficient printable solar cells," ACS Energy Lett. **5**, 1386 (2020).

[30] S. G. Kim, J. H. Kim, P. Ramming, Y. Zhong, K. Schötz, S. J. Kwon, S. Huettner, F. Panzer, and N. G. Park, "How antisolvent miscibility affects perovskite film wrinkling and photovoltaic properties," Nat. Commun. **12**, 1554 (2021).

[31] S. Shao, M. Abdu-Aguye, L. Qiu, L. H. Lai, J. Liu, S. Adjokatse, F. Jahani, M. E. Kamminga, G. H. Ten Brink, T. Palstra, B. J. Kooi, J. C. Hummelen, and M. Antonietta Loi, "Elimination of the light soaking effect and performance enhancement in perovskite solar cells using a fullerene derivative," Energy Environ. Sci. **9**, 2444 (2016).

[32] Q. Chen, J. Luo, R. He, H. Lai, S. Ren, Y. Jiang, Z. Wan, W. Wang, X. Hao, Y. Wang, J. Zhang, I. Constantinou, C. Wang, L. Wu, F. Fu, and D. Zhao, "Unveiling roles of tin fluoride additives in high-efficiency low-bandgap mixed tin-lead perovskite solar cells," Adv. Energy Mater. **11**, 2101045 (2021).

[33] K. D. G. I. Jayawardena, R. M. I. Bandara, M. Monti, E. Butler-caddle, T. Pichler, H. Shiozawa, Z. Wang, S. Jenatsch, S. J. Hinder, M. G. Masteghin, M. Patel, H. M. Thirimanne, W. Zhang, R. A. Sporea, J. Lloyd-Hughesb, and S. R. P. Silva, "Approaching the Shockley–Queisser limit for fill factors in lead–tin mixed perovskite photovoltaics," J. Mater. Chem. A **8**, 693 (2020).

[34] Q. Shang, Y. Wang, Y. Zhong, Y. Mi, L. Qin, Y. Zhao, X. Qiu, X. Liu, and Q. Zhang, "Unveiling structurally engineered carrier dynamics in hybrid quasi-two-dimensional perovskite thin films toward controllable emission," J. Phys. Chem. Lett. **8**, 4431 (2017).

[35] J. Liu, J. Leng, K. Wu, J. Zhang, and S. Jin, "Observation of internal photoinduced electron and hole separation in hybrid two-dimensional perovskite films," J. Am. Chem. Soc. **139**, 1432 (2017).

[36] D. S. Lee, J. S. Yun, J. Kim, A. M. Soufiani, S. Chen, Y. Cho, X. Deng, J. Seidel, S. Lim, S. Huang, and A. W. Y. Ho-Baillie, "Passivation of grain boundaries by phenethylammonium in formamidinium-methylammonium lead halide perovskite solar cells," ACS Energy Lett. **3**, 647 (2018).

[37] J. Dong, S. Shao, S. Kahmann, A. J. Rommens, D. Hermida-Merino, G. H. ten Brink, M. A. Loi, and G. Portale, " Mechanism of crystal formation in Ruddlesden–Popper Sn-based perovskites," Adv. Funct. Mater. **30**, 2001294 (2020).

[38] C. C. Boyd, R. C. Shallcross, T. Moot, R. Kerner, L. Bertoluzzi, A. Onno, S. Kavadiya, C. Chosy, E. J. Wolf, J. Werner, J. A. Raiford, C. de Paula, A. F. Palmstrom, Z. J. Yu, J. J. Berry, S. F. Bent, Z. C. Holman, J. M. Luther, E. L. Ratcliff, N. R. Armstrong, and M. D. McGehee, "Overcoming redox reactions at perovskite-nickel oxide interfaces to boost voltages in perovskite solar cells," Joule **4**, 1759 (2020).

[39] M. Jung, T. J. Shin, J. Seo, G. Kim, and S. Il Seok, " Structural features and their functions in surfactantarmoured methylammonium lead iodide perovskites for highly efficient and stable solar cells," Energy Environ. Sci. **11**, 2188 (2018).

[40] X. Jia, L. Zhang, Q. Luo, H. Lu, X. Li, Z. Xie, Y. Yang, Y. Q. Li, X. Liu, and C. Q. Ma, "Power conversion efficiency and device stability improvement of inverted perovskite solar cells by using a ZnO:PFN composite cathode buffer layer," ACS Appl. Mater. Interfaces **8**, 18410 (2016).

[41] A. F. Castro-Méndez, J. Hidalgo, and J. P. Correa-Baena, "The role of grain boundaries in perovskite solar cells," Adv. Energy Mater. **9**, 1901489 (2019).

[42] Z. Chu, M. Yang, P. Schulz, D. Wu, X. Ma, E. Seifert, L. Sun, X. Li, K. Zhu, and K. Lai, "Impact of grain boundaries on efficiency and stability of organic-inorganic trihalide perovskites," Nat. Commun. **8**, 2230 (2017).

[43] J. W. Lee, S. H. Bae, N. De Marco, Y. T. Hsieh, Z. Dai, and Y. Yang, "The role of grain boundaries in perovskite solar cells," Mater. Today Energy **7**, 149 (2018).

[44] Y. Zhou, Y. Yin, X. Zuo, L. Wang, T. Li, Y. Xue, A. Subramanian, Y. Fang, Y. Guo, Z. Yang, M. Cotlet, C. Nam, and M. H. Rafailovich, "Improving thermal stability of perovskite solar cells by suppressing ion migration using copolymer grain encapsulation," Chem. Mater. **33**, 6120 (2021).

[45] I. van de Riet, H. H. Fang, S. Adjokatse, S. Kahmann, and M. A. Loi, "Influence of morphology on photoluminescence properties of methylammonium lead tribromide films," J. Lumin. **220**, 117033 (2020).

[46] H. H. Fang, F. Wang, S. Adjokatse, N. Zhao, and M. A. Loi, "Photoluminescence enhancement in formamidinium lead iodide thin films," Adv. Funct. Mater. **26**, 4653 (2016).

[47] S. Shao, M. Abdu-Aguye, T. S. Sherkar, H. H. Fang, S. Adjokatse, G. ten Brink, B. J. Kooi, L. J. A. Koster, and M. A. Loi, "The effect of the microstructure on trap-assisted recombination and light soaking phenomenon in hybrid perovskite solar cells," Adv. Funct. Mater. **26**, 8094 (2016).

[48] W. Ke, I. Spanopoulos, Q. Tu, I. Hadar, X. Li, G. S. Shekhawat, V. P. Dravid, and M. G. Kanatzidis, "Ethylenediammonium-based 'Hollow' Pb/Sn perovskites with ideal band gap yield solar cells with higher efficiency and stability," J. Am. Chem. Soc. **141**, 8627 (2019).

[49] Z. Jiang, "GIXSGUI: A MATLAB toolbox for grazing-incidence x-ray scattering data visualization and reduction, and indexing of buried three-dimensional periodic nanostructured films," J. Appl. Crystallogr. **48**, 917 (2015).